

Arctic Ocean mixed-layer eddy generation under leads in sea ice

David C. Smith IV

Department of Mechanical and Aerospace Engineering, Arizona State University, Tempe, Arizona, USA

J. W. Lavelle

Pacific Marine Environmental Laboratory, NOAA, Seattle, Washington, USA

H. J. S. Fernando

Department of Mechanical and Aerospace Engineering, Arizona State University, Tempe, Arizona, USA

Received 26 January 2001; revised 13 June 2001; accepted 9 November 2001; published 13 August 2002.

[1] Convection in the Arctic Ocean mixed layer occurs under openings in sea ice where new sea ice is formed. The process of brine rejection during ice formation creates negatively buoyant fluid at the surface of ice leads. When the fluid convects downward the ocean mixed layer below the lead is stirred vertically and, through planetary rotational effects, along-lead flows at the lead edges are induced. These vertical and lateral motions have been previously studied using two-dimensional numerical ocean models and observed in field programs such as LeadEx. In this paper the generation of Arctic Ocean eddies through dynamic instabilities is investigated using a three-dimensional, nonhydrostatic ocean model. Results suggest that salt-enriched vortices can develop at the base of the mixed layer as a consequence of brine rejection, but the vortex formation requires a time period of several days, a time long enough that the progenitor lead would likely have closed. The scale of the eddies is found to depend on the magnitude of the buoyancy forcing, the width of the lead, and the duration of the buoyancy forcing. The number of vortices produced depends on lead width and duration of buoyancy forcing but is less sensitive to the magnitude of the buoyancy forcing. Vortex sizes, scaled appropriately, and vortex numbers are compared with those found in recent laboratory studies of convectively driven flows from line segment sources.

INDEX TERMS: 4207 Oceanography: General: Arctic and Antarctic oceanography; 4255 Oceanography: General: Numerical modeling; 4540 Oceanography: Physical: Ice mechanics and air/sea/ice exchange processes; 4520 Oceanography: Physical: Eddies and mesoscale processes; 4572 Oceanography: Physical: Upper ocean processes; **KEYWORDS:** convection, Arctic mixed layer, leads, numerical study

1. Introduction

[2] Leads are long, narrow cracks in sea ice in the Arctic pack ice. They are transient features that occupy a small percentage of the ice-open water fraction at any given time. A given lead typically exists for a period <24 hours and has a width of $O(100\text{--}1000\text{ m})$. The ice-open water fraction typically represented by leads ranges from 1% to 10%. Their climatic importance, however, lies in the role that they play in air-sea transfers that are otherwise limited by the presence of ice.

[3] During winter the rate of air-sea transfer of heat through leads from the Arctic Ocean to the overlying atmosphere can range up to several hundred W m^{-2} . This heat flux cools the Arctic Ocean mixed layer and heats the overlying atmospheric boundary layer. Because of the limited spatial and temporal nature of this important process, however, climate and general circulation models fail to

properly resolve these processes. Instead, these models must rely on their representation as subgrid scale processes. Typically, models represent air-sea heat exchange by a weighted average of ice-air and open water-air exchange terms based on the percentage of open water. Effects of convectively driven circulations would be represented in coarse resolution climate models by eddy-mixing terms in the upper ocean or lower atmosphere. Such a representation clearly provides little information about important convective events that occur in both the ocean and atmosphere. Improved understanding of these events will lead to improved parameterization of them in these large-scale models. We focus here on the upper ocean eddy variability associated with leads in sea ice.

[4] In this paper we will examine the three-dimensional response of a nonhydrostatic ocean model to buoyancy forcing under a single lead in sea ice. These results build on several previous papers in which the two-dimensional response was studied. The emphasis in this three-dimensional study is on along-lead variability and the potential for mixed-layer eddy generation by convection in leads.

2. Previous Studies

[5] Studies of convective circulation cells in initially homogeneous, two-layer, and continuously stratified fluids have been reported in numerous previous publications. Most investigations have focused on convection from point sources or circular distributed sources and most in non-rotating [e.g., *Morton et al.*, 1956] rather than rotating [*Helfrich and Battisti*, 1991; *Jones and Marshall*, 1992] background environments.

[6] The lead problem is fundamentally one of convection in a shallow, homogeneous, rotating environment from a source that has an elongated rectangular area. Previous studies have shown, for example, that the presence of the Arctic halocline serves as an impenetrable barrier for sinking plumes [*Kozo*, 1983]. Plumes impinging on the interface may drive internal wave variability but are forced to spread laterally across the upper interface. We thus regard lead plumes as basically confined to the unstratified ocean surface mixed layer, typically having layer thickness H on the order of 50 m thick. Since leads are typically kilometers in length L and many hundreds of meters wide W , the convection region must be considered to be a shallow one. Because $H \ll W \ll L$, the source cannot be viewed as a line or line segment source. From a practical point of view a source can be considered to be a line only if source $W \ll H$. For the source to be a line segment source one additional condition is required: $W \ll L$. If that second condition is untrue and $W \cong L \ll H$ the source should be considered more of a point source. Although the Arctic lead, in contrast to point, line, or line segment source cases, is a distributed source problem, we will look to the reports of laboratory line segment plume experiments [*Noh et al.*, 1992; *Ching et al.*, 1993; *Fernando and Ching*, 1993; *Bush and Woods*, 1999] to offer suggestions on ways to scale, after modification for lead width, results of these simulations. Numerical simulations and laboratory experiments exist for other distributed source cases [*Jones and Marshall*, 1992; *Maxworthy and Narimousa*, 1994; *Colomer et al.*, 1999; *Fernando and Smith*, 2001], but the fact that Arctic lead convection occurs in a shallow environment makes this case much different than those.

[7] We adopt the notation of previous studies. Total source buoyancy flux F_0 [e.g., *Turner*, 1973] and the total volume flux of fluid at the source Q are related by

$$F_0 = g \frac{\Delta \rho}{\rho} Q, \quad (1)$$

where the subscript zero denotes a value at the source level. The buoyancy flux per unit area at the source B_0 [*Turner*, 1973] and F_0 are related by source area $A = WL$:

$$B_0 = \frac{F_0}{WL}, \quad (2)$$

where W is the lead width and L is the lead length.

[8] Buoyancy flux per unit length of source, a value often cited in line and line segment cases, is thus either $B_0 W$ or $F_0 L^{-1}$. Unless otherwise noted, we refer to buoyancy flux per unit area B_0 as buoyancy flux.

[9] A simple equation of state relates density ρ to salinity S in the mixed layer:

$$\rho = \rho_0(1 + \alpha S), \quad (3)$$

where ρ_0 is a reference density (1000 kg m^{-3}), and α , the salinity expansion coefficient, is equal to $8.08 \times 10^{-4} \text{ psu}^{-1}$. No temperature dependence has been included in equation (3) because at temperatures near the freezing point, density variations are more dependent on salinity than on temperature [*Morison*, 1980].

[10] The density contrast of the source layer and the ambient fluid can be calculated using equation (3), from which reduced gravity

$$g' = g\alpha\Delta S \quad (4)$$

can be evaluated, where ΔS is the salinity in excess of the background salinity. Creating a pseudo volume flux at the source from the product of source area and the areal averaged vertical velocity just below the source, w , yields

$$Q = wA = wWL. \quad (5)$$

With a brine rejection rate F_S approximated by

$$F_S = \rho_0 w \Delta S, \quad (6)$$

the relationship between B_0 and F_S becomes

$$B_0 = g w \alpha \Delta S = \frac{g \alpha F_S}{\rho_0}. \quad (7)$$

In experiments to follow, the value of B_0 will be made consistent with the value of F_S measured during the LeadEx experiments.

[11] *Bush and Woods* [1999], as we have, find that descending plumes break up into a number of vortices. The resulting eddy scale should be related to the anticipated scale of instability along the density front [*Griffiths et al.*, 1982]. That scale is the Rossby radius of deformation R_d :

$$R_d = (g'h)^{1/2}/f, \quad (8)$$

where f is the rate of rotation. *Bush and Woods* [1999] find that the observed eddy radius r_e is proportional to R_d after it is rewritten in terms of B_0 , W , and f :

$$r_e = (1.6 \pm 0.2) \frac{(B_0 W)^{1/3} t_s^{1/3}}{f^{2/3}}, \quad (9)$$

where t_s is the duration of the buoyancy source. The composite variable $B_0 W$ is the width-averaged buoyancy flux from the source. In the *Bush and Woods* [1999] experiments, W did not vary, so in their analysis, $B_0 W$ was a single variable. It remains to be seen if the same dependence (equation (9)) holds true when B_0 and W are, in fact, independent variables. For typical lead conditions, t_s is $\sim 1 \times 10^5 \text{ s}$ (1 day), B_0 is $2 \times 10^{-7} \text{ m}^2 \text{ s}^{-3}$, W is $\sim 1 \text{ km}$, f is $1 \times 10^{-4} \text{ s}^{-1}$, and eddy radius (equation (9)) is $\sim 2\text{--}4 \text{ km}$. Alternately, evaluating R_d (equation (8)) directly

from our model output using the maximum observed g' value results in a Rossby radius of deformation of 1500 m.

[12] *Bush and Woods* [1999] further argued that the number of coherent anticyclonic vortices n that emerge in the convection process is given by

$$n = 0.3 \frac{Lf^{2/3}}{(B_0 W)^{1/3} t_s^{1/3}}. \quad (10)$$

For the same typical lead conditions when $L \sim 12$ km (in numerical experiments here), n is on the order of 4. Because *Bush and Woods* [1999] employ a constant narrow line source, their experiments were not designed to examine the role of source width W in resulting eddy motions. In this work we will look for the importance of lead width W in these eddy scale considerations.

[13] Previous studies of **deep convection** have used a vertical length scale

$$z_c = l_{\text{rot}} = \left(\frac{B_0}{f^3} \right)^{1/2} \quad (11)$$

to quantify the effect of planetary rotation on convective motions [*Jones and Marshall*, 1992; *Whitehead et al.*, 1996]. When the convective motion reaches a depth z of $\cong 10z_c$ the descent of convecting fluid is arrested by rotation, but $10z_c$ is generally deeper than typical ocean depths [*Maxworthy*, 1997]. For typical Arctic conditions previously listed, $10z_c$ is ~ 3 km, very much larger than the mixed layer depth H . Hence plumes descending from leads are arrested by the pycnocline rather than by rotational effects.

[14] Rotational effects are important in the lateral evolution, however. Over multiple rotation periods the lateral spreading of fluid across the top of the halocline is rotationally modified through the geostrophic adjustment process. These primary differences between shallow Arctic lead convection and oceanic deep convection indicate that different parameterizations for shallow and open-ocean deep convection will likely result.

[15] The breakdown of descending plumes into rotationally organized flows results in three-dimensional circulations. Studies of convection forced in discrete patches have illustrated that baroclinic instability of the rotationally adjusted rim current surrounding the convecting plumes leads to breakdown and spreading of the convective region. [*Send and Marshall* [1995], *Visbeck et al.* [1996], and *Whitehead et al.* [1996] apply *Eady's* [1949] baroclinic instability model to estimate a timescale, t_{Eady} , for this process to occur which relates eddy breakdown time to depth of the convective mixed layer H , the buoyancy forcing B_0 , and rotation f . Owing to the relatively shallow nature of the Arctic mixed layer ($H = O(50 \text{ m})$), the timescale for lead convection is relatively short ($t_{\text{Eady}} \approx 9000 \text{ s}$ (2–3 hours)). This suggests that eddy breakdown along the lead can occur on timescales shorter than the period during which the lead convection is forced ($t_s \sim 24$ hours). In the context of convection forced from line sources, *Bush and Woods* [1999] (discussed further in section 4.7) argue that one should expect a series of anticyclonic eddies under line plumes when $t_{\text{Eady}} < t_s$.

[16] The importance of this instability process in lateral exchange has been emphasized in deep convection studies [*Send and Marshall*, 1995]. Since the eddies generated by this process may exist long after the lead forcing has ceased, this may be a mechanism for redistributing salt farther from its origin than in the absence of rotation, where gravitational spreading and turbulent diffusion would limit the lateral transport. In problems where the forcing occurs over a longer period of time than in leads this lateral spreading can approximately balance the production of negatively buoyant fluid at the surface of the forcing region. *Chapman and Gawarkiewicz* [1996] argue that this may lead to a steady state balance in coastal polynyas over a sloping bottom. Given the short duration of lead-associated buoyancy forcing, it seems unlikely that any kind of steady balance can exist between lateral spreading and the buoyancy source in lead convection.

3. Model Description

[17] The model used in this study is a three-dimensional extension of that used by *Smith and Morison* [1998], where a more detailed description of its formulation can be found. It is a nonhydrostatic, finite difference model for convective flow in a rectangular domain, based on momentum equations for an incompressible Boussinesq fluid

$$\frac{\partial \mathbf{u}}{\partial t} + \mathbf{u} \cdot \nabla \mathbf{u} + \frac{1}{\rho_0} \nabla p + f \mathbf{k} \times \mathbf{u} = \mathbf{F}_{\text{DISS}} - \frac{\mathbf{k} g \rho}{\rho_0}. \quad (12)$$

[18] Conservation of salt is expressed by

$$\frac{\partial (S)}{\partial t} + \mathbf{u} \cdot \nabla (S) = \mathbf{F}_{\text{DIFF}} + Q_s. \quad (13)$$

The source term Q_s distributes salt over a rectangular area in a thin layer several grid cells thick [e.g., *Smith and Morison*, 1998] near the surface. An exponential z -dependence, given the source in these cases, had an e -folding length λ_s of 5 m,

$$Q_s = \frac{F_s}{\rho_0 \lambda_s} e^{-(z/\lambda_s)}. \quad (14)$$

The salt flux F_s in the reference experiment (experiment 1) was given a value of $2 \times 10^{-5} \text{ mg kg}^{-1} \text{ s}^{-1}$ on the basis of lead observations reported by *Morison and McPhee* [1998]. These equations are augmented by the continuity equation for incompressible fluid:

$$\nabla \cdot \mathbf{u} = 0 \quad (15)$$

and by a simple equation of state (3).

[19] The solution procedure involves taking the divergence of the momentum equations and using the continuity equation, resulting in a three-dimensional Poisson equation for pressure which is solved each model time step. The solution method originated with *Harlow and Welch* [1965]. All equations were time-integrated using the leapfrog method. Equations (12) and (13) were approximated by center differencing.

[20] The equations were integrated in a domain with rigid boundaries having physical dimensions in meters of $30,000 \times 30,000 \times H$. The value of H was typically 45 m,

Table 1. Experimental Parameters and Summary of Eddy Scales^a

Experiment	H , m	W , m	B_0 , $\text{m}^2 \text{s}^{-3}$	$B_0 W$, $\text{m}^3 \text{s}^{-3}$	t_s , days	λ_L , m	r_e^b , m	L_e^c	n
1	45	720	2×10^{-7}	1.4×10^{-4}	1	0	1744	1500	4
2	45	720	4×10^{-7}	2.9×10^{-4}	1	0	2197	2653	4
3	45	720	8×10^{-7}	5.8×10^{-4}	1	0	2768	3625	3
4	45	1440	2×10^{-7}	2.8×10^{-4}	1	0	2168	2125	5
5	45	2880	2×10^{-7}	5.8×10^{-4}	1	0	2734	2531	8
6	45	5760	2×10^{-7}	1.1×10^{-3}	1	0	3441	2825	8
7	45	720	2×10^{-7}	1.4×10^{-4}	2	0	2203	1781	4
8	45	720	2×10^{-7}	1.4×10^{-4}	4	0	2768	1638	10
9	45	720	2×10^{-7}	1.4×10^{-4}	8	0	3440	1363	10
10	200	720	2×10^{-7}	1.4×10^{-4}	1	0	1384	^d	^d
11	800	720	2×10^{-7}	1.4×10^{-4}	1	0	1384	^d	^d
12	45	720	2×10^{-7}	1.4×10^{-4}	1	7680	1744	1781	4
13	45	720	2×10^{-7}	1.4×10^{-4}	1	3840	1744	1583	3
14	45	720	2×10^{-7}	1.4×10^{-4}	1	1920	1744	1250	1

^aExperiments 1–14 employ biharmonic mixing; experiment 15 (Figure 9) utilizes Smagorinsky mixing.

^bValues taken from *Bush and Woods* [1999], equation (9).

^cValues based on the 31.04 contour at $z = -37.5$ m.

^dExperiments 10 and 11 with increased layer thickness values H produced comparable numbers and distributions of eddies as experiment 1. The maximum salt anomaly near the bottom, however, is much weaker, making the definition of eddy radius in terms of the 31.04 contour inapplicable.

but larger values were also used. The model domain was divided into $128 \times 128 \times 10$ cells, making cell sizes of $\Delta x = 240$ m and $\Delta z = 5$ m. This resolution is much coarser than that used in the previous two-dimensional studies [Smith and Morison, 1998] but is determined by computational practicality and by the larger scales of eddy formation associated with along-lead variability. The receiving fluid was initially homogeneous and quiescent. In these experiments the lead is stationary, although it is important to point out that this is not necessarily the case in Arctic leads where the ice and the buoyancy source are moving relative to the upper ocean.

[21] The model time step was 64 s. The duration of simulations in all cases was 8 days. This time is long enough to examine possible eddy generation for a given lead geometry but not spin-down. One might expect that over the time of eddy spin-down (O (months)), the eddy would drift away from the source region. The larger computational domains required to study that problem were not realizable.

[22] The independent variables in the experiments (Table 1) were W , H , B_0 , and t_s . The source length L was fixed at 12 km, and the angular rotation rate was set at $7.27 \times 10^{-5} \text{ s}^{-1}$. W varied in four steps from 720 to 5760 m. H ranged from 45 to 800 m. The values assigned to B_0 , ranging from 2×10^{-7} to $8 \times 10^{-7} \text{ m}^2 \text{ s}^{-3}$, were chosen so that the corresponding F_S would be commensurate with observations made during the LeadEx field program. B_0 was constant between $0 < t < t_s$ and was zero thereafter. The salt flux from ice may be time-dependent, but the focus here is on the basic features of multiple eddy formation. Other numerical studies that focus on the coupled ice-ocean system in leads [Ou, 1988] have investigated aspects of time-dependent source and other aspects of ice motion in the lead system. The variable t_s typically was given a value of 1 day, but it ranged from 1 to 8 days.

[23] To represent subgrid scale-mixing processes, the model relies on constant eddy dissipation and diffusion in the form of biharmonic coefficients (experiments 1–13) or coefficients generated by the Smagorinsky mixing scheme. In the biharmonic experiments, \mathbf{F}_{DISS} and \mathbf{F}_{DIFF} take the

form $-B_h \nabla^4 \mathbf{u}$ and $-B_s \nabla^4 S$, respectively. In the horizontal directions where the grid resolution was 240 m the biharmonic mixing coefficients for momentum and salt, B_h and B_s , respectively, were set at $2 \times 10^4 \text{ m}^4 \text{ s}^{-1}$. These choices of coefficients result in spin-down times for typical eddy length scales that are much longer than the duration of the present experiments. In the vertical the same mixing coefficients were reduced by the ratio $(\Delta z / \Delta x)^4$ to account for the aspect ratio $(\Delta z / \Delta x)$ of the grid cells. Shear-dependent mixing of the Smagorinsky type [e.g., Lavelle and Smith, 1996] was also employed. In those experiments, \mathbf{F}_{DISS} and \mathbf{F}_{DIFF} take the form $\nabla \cdot A_I \nabla$ and $\nabla \cdot K_I \nabla$, respectively. The coefficients A_I and K_I are determined by the Smagorinsky mixing routine, which is discussed in section 4.8. Results from one experiment of that type are presented to highlight similarities and differences with results from the biharmonic mixing cases.

4. Results

[24] In the following sections we show the time evolution of a reference experiment and show how variations in model parameters affect the resulting flow circulations with emphasis on the resulting eddy scales. Table 1 provides a quantitative summary of the resulting eddy radius (r_e) and number of eddies (n) and allows for intercomparison of experimental eddy scales and the scale r_e predicted by *Bush and Woods* [1999].

4.1. Reference Experiment

[25] The temporal evolution of salinity and vorticity in the reference experiment (experiment 1) is shown in Figures 1 and 2. Snapshots are shown from an 8-day simulation, a time which is long compared with the rotation period (24 hours) and with the time over which buoyancy forcing has been applied (24 hours). This long time span allows the plumes to detach from the surface and multiple vortices to spin up. Our previous numerical experiments with line plumes [Lavelle and Smith, 1996] did not uncover multiple vortex formation, primarily because those experiments did not extend over sufficient rotation periods.

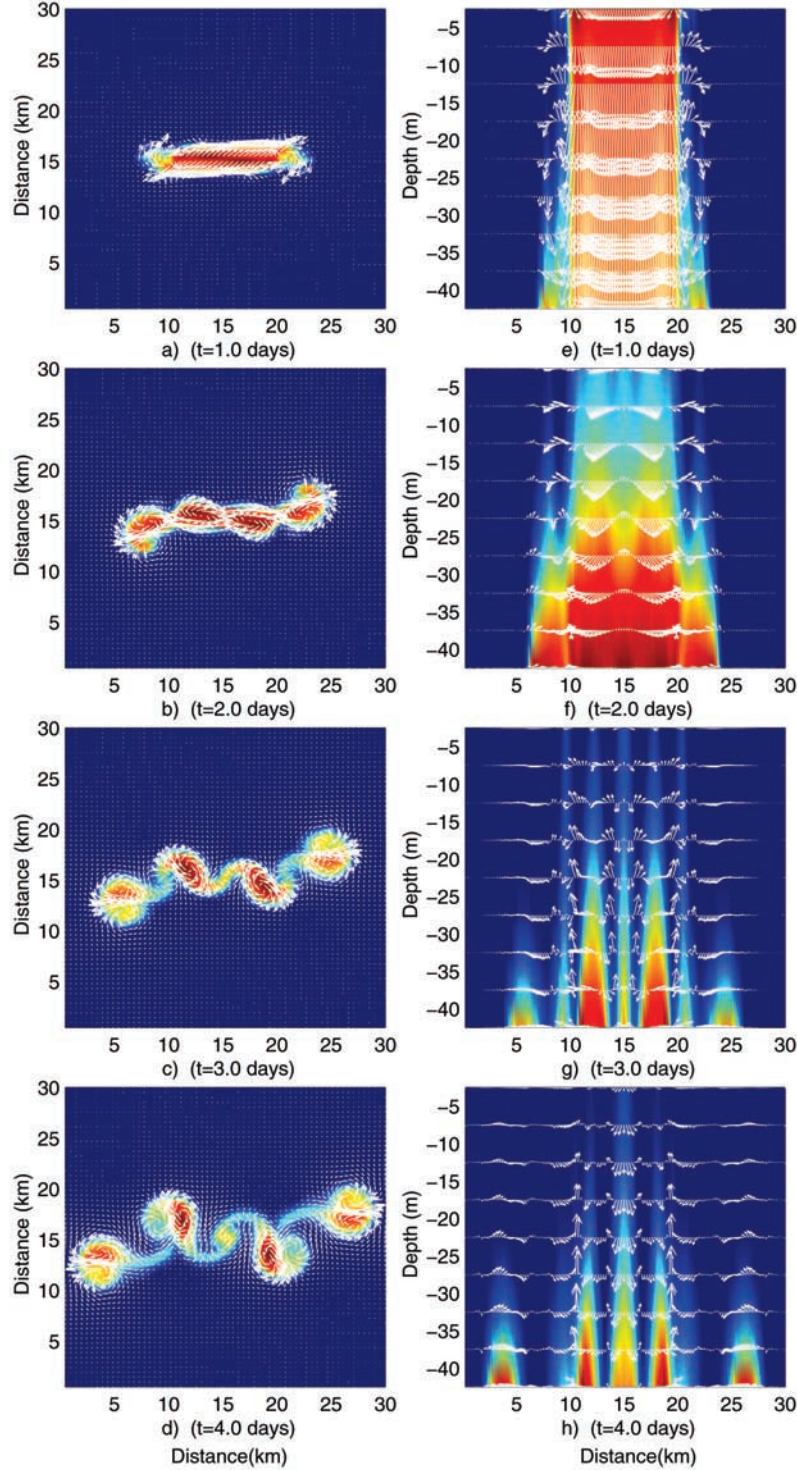


Figure 1. The reference experiment (experiment 1, Table 1). (a–d) Salinity anomaly at $z = -37.5$ m at $t = 1, 2, 3$, and 4 days. (e–h) Salinity anomaly at $y = 15$ km (centerline) at $t = 1, 2, 3$, and 4 days. In all panels, ΔS ranges from 0.001 (blue) to 0.07 (red). In this and in subsequent horizontal vector fields, only half of the model vectors are shown; that is, every other vector in the x, y directions has been eliminated for presentation purposes. Vertical vectors are scaled by a factor of 2X (Figure 1e), 5X (Figure 1f), and 10X (Figure 1g), relative to vector size 1X in Figure 1d.

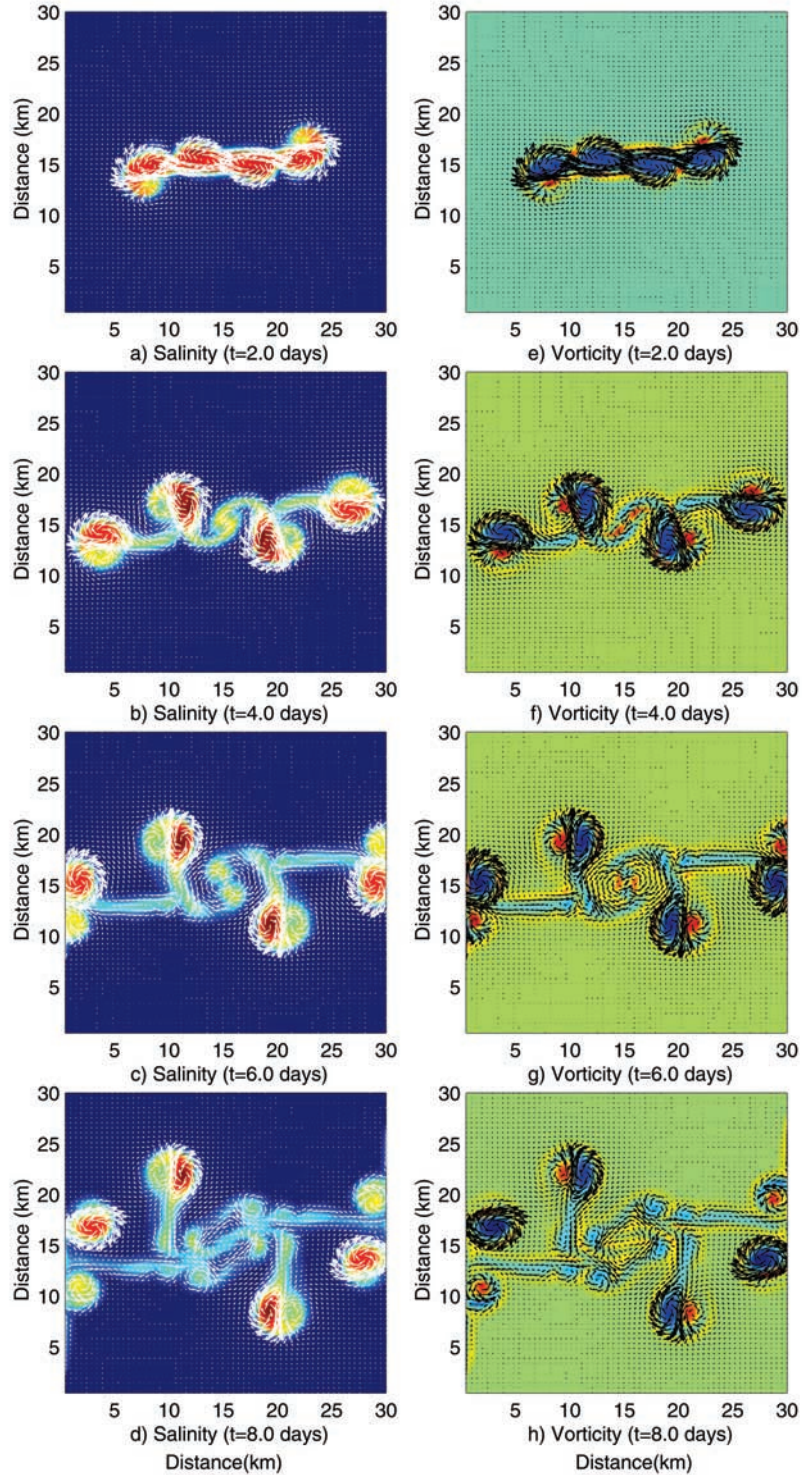


Figure 2. The reference experiment (experiment 1, Table 1). (a–d) Salinity anomaly at $z = -37.5$ m at $t = 2, 4, 6$, and 8 days. The concentration range is as in Figure 1. (e–h) Relative vorticity ζ (s^{-1}) in the z -direction at $y = 15$ km (source centerline) at $t = 2, 4, 6$, and 8 days. Values for ζ range from $-2.5 \times 10^{-4} \text{ s}^{-1}$ (blue) to $3.0 \times 10^{-4} \text{ s}^{-1}$ (red).

[26] The evolution of the salt field over the first 4 days is shown in Figure 1. Circulation is convergent/cyclonic at the surface and divergent/anticyclonic near the bottom at $z = -37.5$ m, where the descending plumes spread outward

across the model-solid bottom boundary. The descending line plume is sheetlike during the forcing period (Figure 1e) but becomes bottom-trapped and anticyclonically sheared (Figure 1f) by day 2. By day 4 the excess salinity is

primarily in four vortices, the vertical scale of which is no more than 20 m.

[27] The vorticity signature (and hence the sense of rotation) of the eddies is shown in vorticity plots (Figure 2). In this case, evolution over 8 days is shown for comparison with subsequent experiments. Two dipole pairs form on day 2 on each end of the line plume, and these propagate ($\sim 1 \text{ km d}^{-1}$) in the along-source ($\pm x$) direction away from their initial formation locations. By day 3 the line plume has separated through instability into discrete rotating plumes, the strongest of which are anticyclones centered at $x = 12$ and $x = 18 \text{ km}$. Maximum horizontal velocities near the bottom are 0.10 m s^{-1} (but average 0.05 m s^{-1}), and maximum salinity anomalies (which are in anticyclonic circulation cells at depth) are $\sim 0.06 \text{ m s}^{-1}$. Maximum vertical velocities are only $8 \times 10^{-3} \text{ m s}^{-1}$.

[28] In this and in subsequent experiments we have estimated a dominant eddy size (Table 1, column 9). The eddy size was estimated graphically from line contour plots as the radius of the 0.04 salinity anomaly contour at a depth of $z = -37.5 \text{ m}$. This process is somewhat subjective as eddy shape varies from circular. The values for eddy radius shown in Table 1 are based on averages taken over the total number of eddies in a given experiment. Where eddy shape is noncircular, major and minor axis values are averaged to obtain a representative eddy scale. The number of resultant eddies is also shown in Table 1. Here again this estimate is subjective, as eddy evolution, merger, and splitting occur during a given experiment.

[29] The resulting eddy size can be compared with the expression for eddy radius (equation (9)) given by *Bush and Woods* [1999]. In this experiment an eddy radius of 1500 m is not much different than that predicted (1744 m) by the *Bush and Woods* [1999] formula. On day 4 these anticyclones evolve into a second dipole pair which forms at each end of the unstable line plume, and these also propagate laterally in the $\pm y$ directions (Figures 1c and 1d). A transient cyclone forms at $x = 15 \text{ km}$ in middomain which has comparable scales to the bottom-trapped anticyclones, but it does not persist in the final 4 days of the simulation. The cyclone forms from the bottom up as upward recirculating flow is vortex-stretched. The radial scale (radius) of the eddies in this simulation is $\sim 1.5 \text{ km}$. In subsequent experiments we will show how this scale varies with lead width, buoyancy flux, and duration of buoyancy forcing. Variations in these parameters result in a range of eddy sizes from 1–3 km for realistic Arctic lead-forcing parameters. The anticyclones are the dominant salt-containing eddies in this and subsequent experiments.

[30] The three-dimensional circulation structure of the eddies seen in Figures 1 and 2 are qualitatively consistent with some aspects of the former two-dimensional simulations of *Smith and Morison* [1993, 1998]. In those simulations, motion near the surface was convergent and cyclonically sheared in descending plumes. Descending high-salinity anomaly plumes accelerated downward to middepth, beyond which the plumes decelerated and outward divergent spreading was deflected anticyclonically by rotation across the bottom. The two-dimensional picture thus suggests that all positive salt anomalies should rotate anticyclonically at depth. Figures 3a–3f show this to be largely the case, with high-salinity cores concentrated in

anticyclones near the bottom. Cyclones with a weak salinity anomaly are interspersed between the anticyclones, but these evolve as ascending motions that stretch fluid columns in vertical recirculations between downward plumes.

[31] The laboratory study of *Bush and Woods* [1999] also suggests that predominantly anticyclonic eddies are produced by unsteady line segment sources. Their results are less indicative of dipole formations, however. A possible explanation for this discrepancy lies in the way in which the laboratory convection is produced, with high-salinity water released from discrete sources at the surface instead of in a continuous line source.

4.2. Sensitivity to Increased Buoyancy Flux

[32] Sensitivity to increased B_0 was examined next. In experiment 2 the buoyancy flux B_0 has been doubled, and in experiment 3, B_0 has been quadrupled over that in experiment 1. Salinity fields at $z = -37.5$ at $t = 4$ days for all three experiments are found in Figures 3a–3c. The effect of increased buoyancy flux is to increase the scale of the unstable wave growth, resulting in slightly larger and fewer eddies (Figures 3a–3c).

[33] As noted in section 4.1, the determination of eddy size involves some imprecision. The exact eddy scale is difficult to determine because in any single experiment, eddies have variable sizes, and furthermore their shapes change (such as the elliptical central anticyclones seen in Figures 3a–3c) over time. Estimates of L_e in Table 1 should be viewed in that light. Nonetheless it is fair to say from Figure 3 that the size of the eddies is larger for increased buoyancy flux. Over the three experiments the radius of eddies ranges from ~ 1.5 to 3.6 km , a larger range than the 1744–2768 m range predicted by equation (9) (Table 1, column 8).

[34] Figures 3d–3f show vertical slices through the model domain for each of these experiments and illustrate the vertical structure of the eddies. They are located in the lower part ($O(10 \text{ m})$) of the mixed layer. In all three experiments the dominant salt-containing vortices are anticyclonic. Velocities (Figures 3d–3f) are primarily horizontal ($O(0.02\text{--}0.1 \text{ m s}^{-1})$ increasing with B_0), though small ($O(2\text{--}6 \times 10^{-4} \text{ m s}^{-1})$) vertical motions persist. The maximum salinity anomaly reaches 0.15 in experiment 3.

4.3. Sensitivity to Lead Width W

[35] Experiments 4, 5, and 6 have progressively larger lead widths in comparison with the reference case (experiment 1): $W = 1440 \text{ m}$ (experiment 4), 2880 m (experiment 5), and 5760 m (experiment 6), respectively. Results at $t = 8$ days and $z = -37.5 \text{ m}$ for all three (Figure 4) should be compared with the corresponding result for experiment 1 (Figure 2). The progression of experiments show that vortex size increases slightly with W , and the number of vortices increases.

[36] The *Bush and Woods* [1999] expression for eddy size (in our notation, equation (9)) indicates that eddy size increases with $B_0 W$ to the one-third power. Wider leads therefore result in larger eddies (Table 1, column 8). Experiments 4 and 5 should have eddy sizes comparable to that in experiments 2 and 3, respectively, where $B_0 W$ is varied by increasing B_0 instead of the lead width W . Since W in

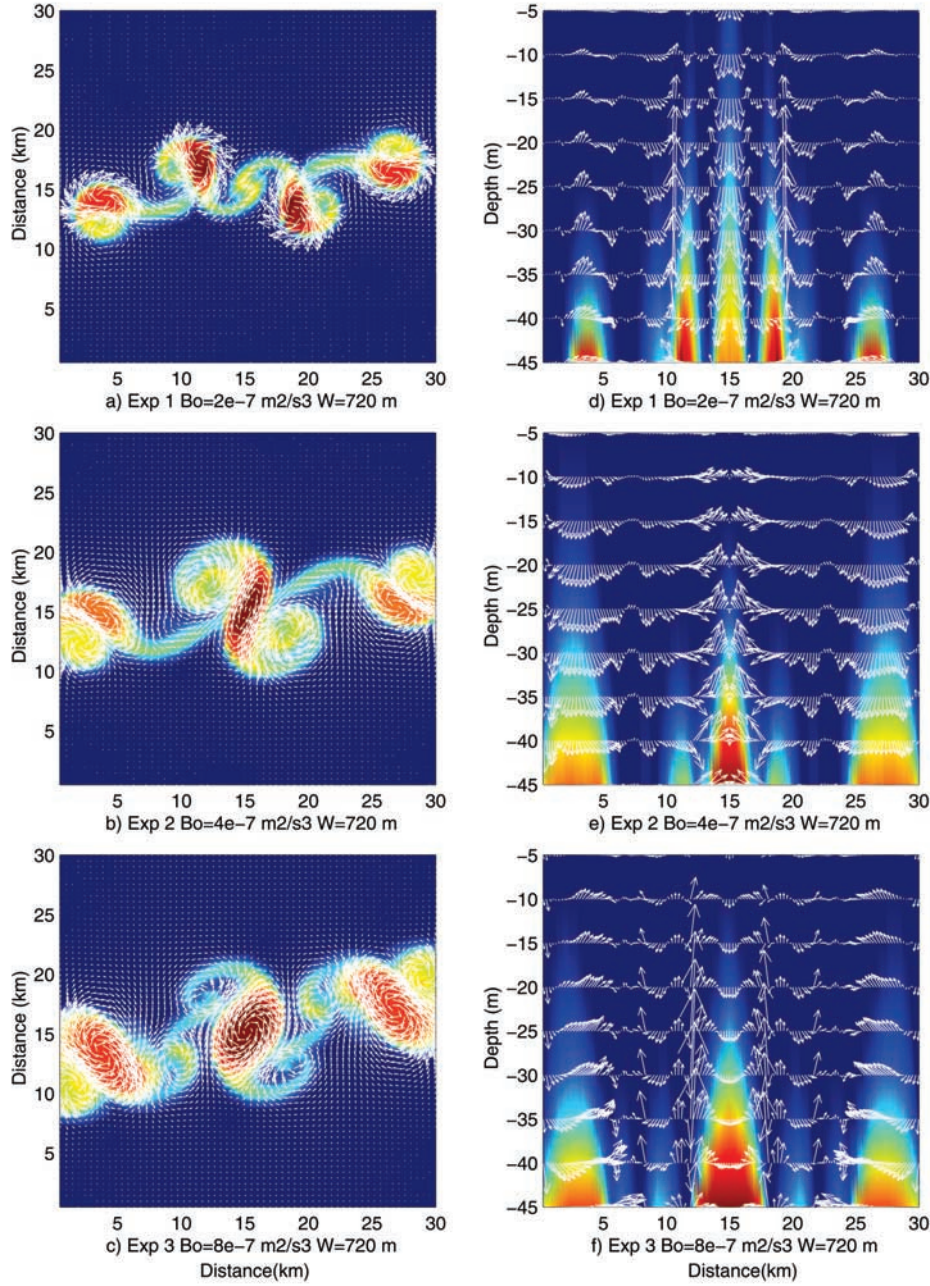


Figure 3. Sensitivity to source buoyancy flux (experiments 1–3). In the left column, salinity anomaly at $z = -37.5$ m and at $t = 4$ days; in the right column, salinity anomaly at $y = 15$ km (source centerline) at $t = 4$ days. (a and d) $B_0 = 2 \times 10^{-7} \text{ m}^2 \text{ s}^{-3}$; (b and e) $B_0 = 4 \times 10^{-7} \text{ m}^2 \text{ s}^{-3}$; (c and f) $B_0 = 8 \times 10^{-7} \text{ m}^2 \text{ s}^{-3}$. ΔS ranges from 0.001 (blue) to 0.07 (Figures 3a and 3d), 0.12 (Figures 3b and 3e), and 0.18 (Figures 3c and 3f) (red).

experiment 6 is 8 times that of experiment 1, one might expect an increase in L_e by a factor of ~ 2 .

[37] Figure 4 shows that eddy sizes increases in these experiments (Table 1) but increases more slowly than predicted by equation (9). The dipole pair that separates off each end of the line source in experiment 1 has a counterpart in experiments 4 and 5 but is not seen in experiment 6. The resulting bottom-trapped, salt-containing anticyclonic eddies in each of these experiments does not

appear to increase significantly in size (2125–2825 m), although the range in size predicted by equation (9) is also not large (2168–3441 m).

[38] One hypothesis regarding the eddy generation is barotropic instability resulting from lateral shear across the line plume. This mechanism would presumably favor increased eddy development when the shear zone (lead width) is narrow, with decreasing energy source for eddies as this width scale is increased. For the range of lead widths

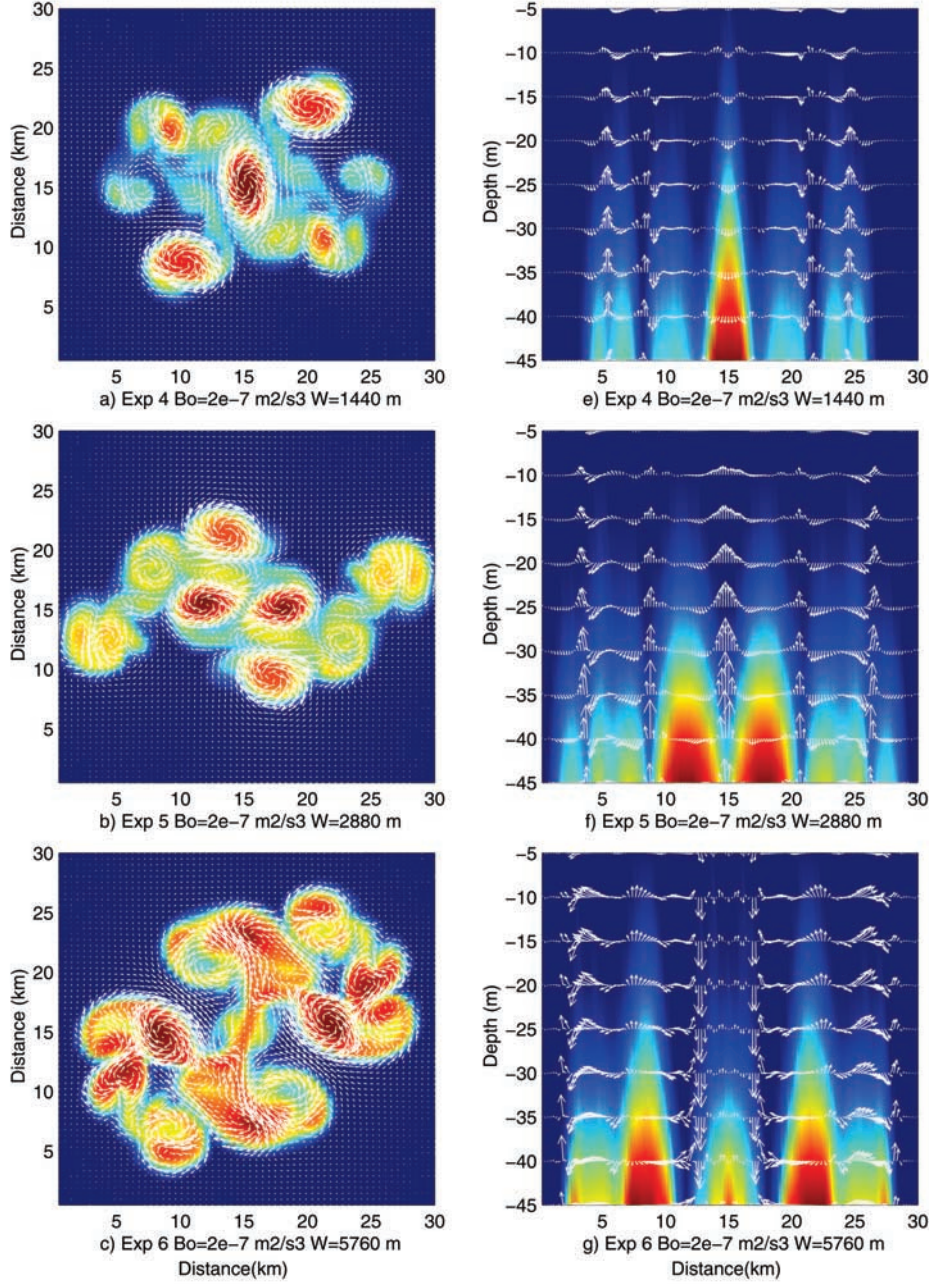


Figure 4. Sensitivity to source width W (experiments 4–6). In the left column, salinity anomaly at $z = -37.5$ m and at $t = 8$ days; in the right column, salinity anomaly at $y = 15$ km (source centerline) at $t = 8$ days. (a and d) $W = 1440$ m; (b and e) $W = 2880$ m; (c and f) $W = 5760$ m. ΔS ranges from 0.001 (blue) to 0.08 (Figure 4a and 4d), 0.09 (Figures 4b and 4e), and 0.09 (Figures 4c and 4f).

considered here this appears not to be the case, with substantial (if less organized) eddy development in experiment 6. This suggests that vertical shear and hence baroclinic instability is equally (if not more) important in setting the eddy scale. The relative roles of barotropic and baroclinic instability in other convection studies is also unclear [Maxworthy, 1997].

[39] Experiment pairs 2 and 4 and 3 and 5 have comparable $B_0 W$ values despite having different B_0 and W values. Equation (9) predicts that the same size of eddy should be

generated in these experiments and, further, that the number of eddies generated should be the same according to the source length arguments of *Bush and Woods* [1999]. The eddy sizes and numbers for these experiments (Table 1) indicate that this is clearly not the case. Eddy size in these experiments is sensitive independently to B_0 and W values and not simply their product. Experiments 4–6 indicate that there is a dependence in the number of eddies on lead width as well as wider leads tend to result in more eddies of comparable size. *Bush and Woods* [1999] obtain the number

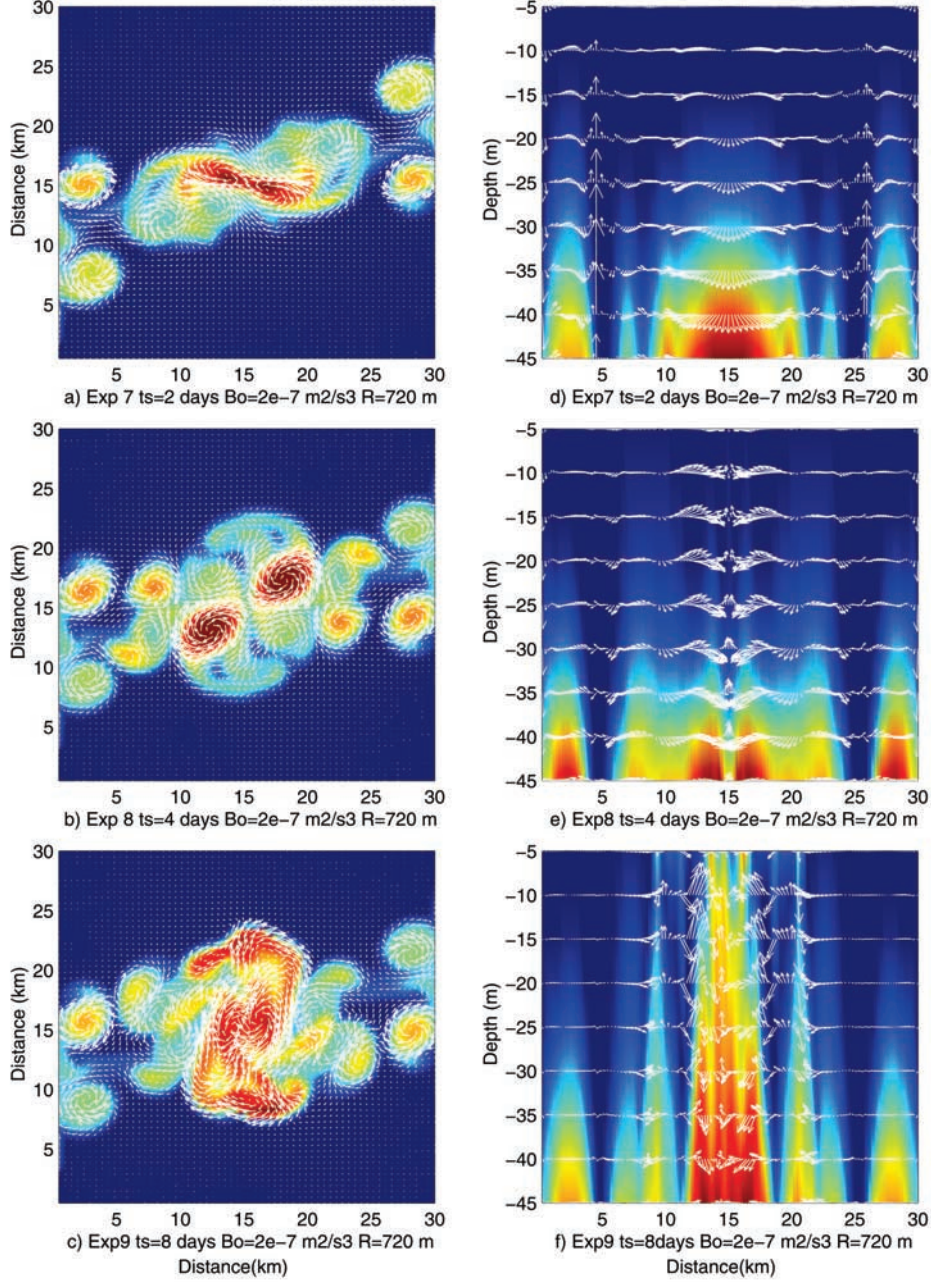


Figure 5. Sensitivity to duration of forcing t_s (experiments 7–9). In the left column, salinity anomaly at $z = -37.5$ m and at $t = 8$ days; in the right column, salinity anomaly at $y = 15$ km (source centerline) at $t = 8$ days. (a and d) $t_s = 2$ days; (b and e) $t_s = 4$ days; (c and f) $t_s = 8$ days. Vertical vectors are scaled by a factor of 15X (Figure 5d) and 7.5X (Figure 5e), relative to vector size 1X in Figure 5f. ΔS ranges from 0.001 (blue) to 0.07 (Figures 5a and 5d), 0.08 (Figures 5b and 5e), and 0.09 (Figures 5c and 5f).

of eddies by dividing the source length by the eddy radius. Our results suggest that dividing the source areal extent by the characteristic eddy scale provides a better estimate.

4.4. Sensitivity to Duration t_s of Buoyancy Source

[40] The experiments discussed thus far have had a single value of buoyancy source time t_s . However, equation (9) indicates that eddy size should be dependent on t_s , with larger eddies produced by increased duration of convective forcing.

Experiments 7–9 repeat experiment 1 ($W = 720$ m, $B_0 = 2 \times 10^{-7} \text{ m}^3 \text{ s}^{-1}$) with t_s increased to 2, 4, and 8 days, respectively. Typically, leads refreeze on timescales < 24 hours, but longer periods of open water may be possible. Equation (9), evaluated for these increased t_s values (Table 1, column 8) indicate that eddy radius should increase to 2203, 2768, and 3440 m, respectively. Hence the range of expected eddy sizes for realistic lead parameters is less than a factor of 2. Figure 5 illustrates salinity plan and profile sections taken at day 8 for

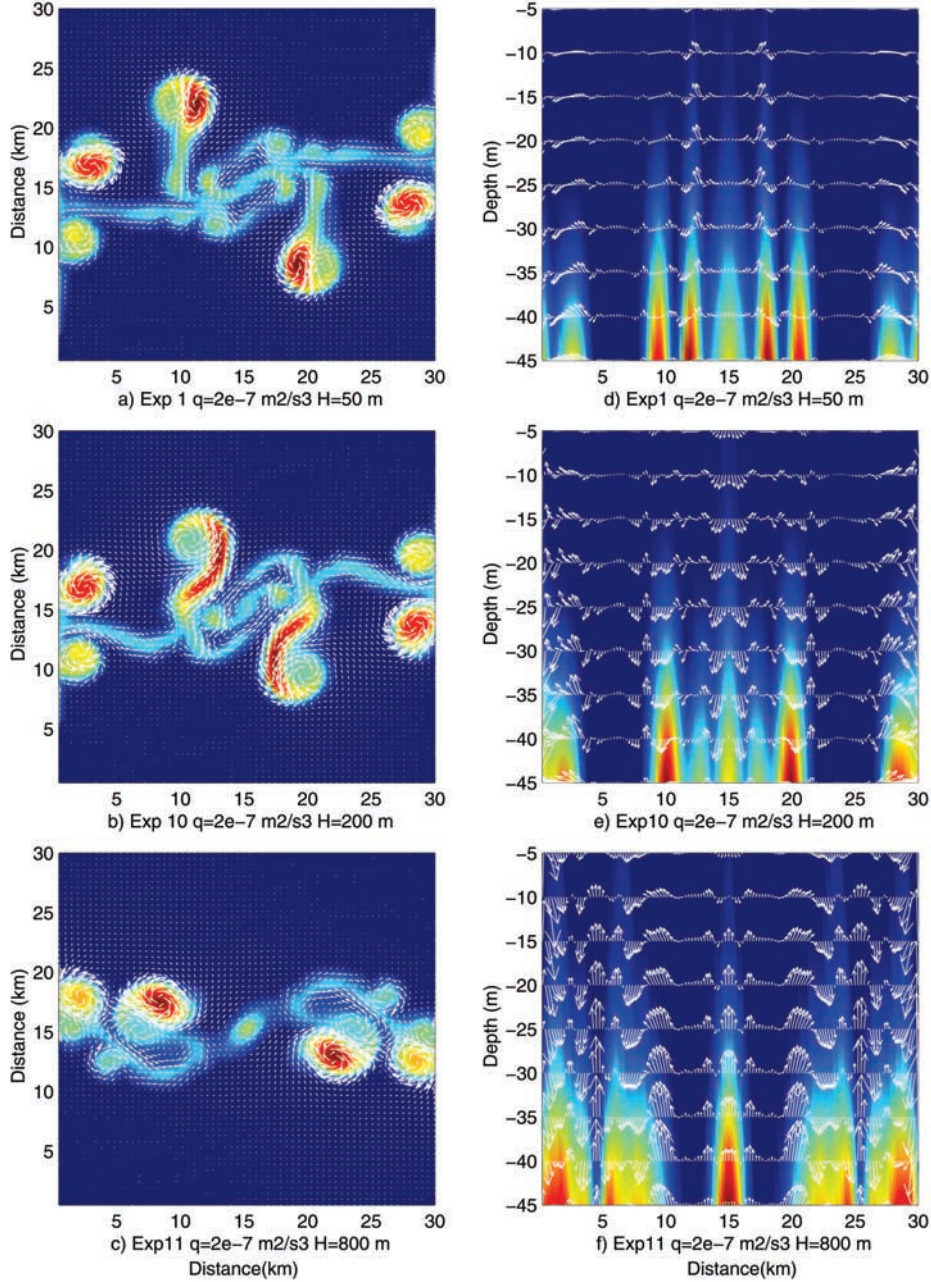


Figure 6. Sensitivity to domain depth H (experiments 1, 10, and 11). In the left column, salinity anomaly at $z = -37.5$ m and at $t = 8$ days; in the right column, salinity anomaly at $y = 15$ km (source centerline) at $t = 8$ days. (a and d) $H = 50$ m; (b and e) $H = 200$ m; (c and f) $H = 800$ m. Vertical vectors are scaled by a factor of 5X (Figure 6d) and 3X (Figure 6e), relative to vector size 1X in panel Figure 6f. ΔS ranges from 0.001 (blue) to 0.07 (Figures 6a and 6d), 0.14 (Figures 6b and 6e), 0.004 (Figures 6c and 6f).

these simulations. A comparison of these experiments indicates that eddy size does not appear to increase with t_s . Instead more (and slightly smaller) eddies are generated as the t_s is increased. A typical cycle of eddy formation in the above experiments is 3–4 days for the generation of bottom-trapped eddies. Experiment 9 (with $t_s = 8$ days) has entered a second cycle of eddy generation, with new eddies generated in the lead, replacing those that have propagated laterally away from the source. The central salinity anomaly in Figure 5f

extends nearly to the surface, indicating this second cycle of eddy generation. The fact that eddy size does not increase with duration of buoyancy forcing as predicted by equation (9) represents the largest difference with the laboratory results of *Bush and Woods* [1999].

4.5. Sensitivity to Domain Depth H

[41] The sensitivity of the results to changes in domain depth is illustrated in Figure 6, where the vertical resolution

is increased to deepen the domain to 200 m (experiment 10, Figure 6b) and 800 m (experiment 11, Figure 6c). The resulting number and sizes of eddies show relatively little sensitivity to these changes. This result is consistent with the formula suggested by *Bush and Woods* [1999] for the eddy scale (equation (9)), which has no dependence on the fluid depth H . Because the descent time for the plumes is much smaller than the rotation period in these cases, the descending plumes are relatively unmodified by rotational effects and have comparable lateral dimensions for the range of depths $H = 45\text{--}800$ m. As *Bush and Woods* [1999] point out, in the limit of $H < 10z_c$ the eddy size is independent of H . These experiments have H values much less than $10z_c = 3000$ m.

4.6. Sensitivity to Along-Lead Perturbations

[42] The simulations discussed in sections 4.1–4.5 pertain to convection from a finite length, straight (line segment) source. Leads have along-lead variability in the ice edge which may trigger other wavelengths of circulation. We would like to know whether other scales of eddies may result when other scales of variability are introduced. This type of simulation was considered by *Akitomo et al.* [1992] in two dimensions. They showed that despite forcing at other scales, the flow organized into flow cells consistent with the Rayleigh Benard prediction.

[43] The basic experiment (experiment 1) was repeated with along-lead variations in lead width. In three separate experiments this wavelength was varied:

$$L = L_0 + A_0 \sin\left(\frac{m\pi\Delta x}{l_{\max}}\right), \quad (16)$$

where $L_0 = 720$ m; $A_0 = 1.2$ km; $m = 8, 16$, and 32 ; and l_{\max} is domain length equaling 30 km. These introduce along-lead wavelengths (λ_L in Table 1) of 7.68 km (experiment 12), 3.84 km (experiment 13), and 1.92 km (experiment 14), respectively. The final day (day 8) of each of these simulations is shown in Figure 7 in plan and profile view. In each of these experiments the final eddy radius is approximately that seen in the experiments discussed above (1–2 km). In experiment 14, where the initial eddy scales are smaller than this, like sign vorticity centers merge between day 4 and 6, producing approximately the same number and sizes of eddies seen, for example, in Figure 4. While it appears that along ice edge variability may serve to trigger the eddy variability and eddies at other scales initially, the eddies evolve rapidly through merger and scale change into eddy fields that closely resemble those seen in the previous straight line source simulations.

4.7. Eddy Scaling

[44] That the resulting eddies should scale with the Rossby radius of deformation (equation (8)) has been found in numerous laboratory and numerical studies [*Griffiths et al.*, 1982; *Bush and Woods*, 1999]. Anticipating that result, *Bush* redefined the Rossby radius of deformation (R_d) using a definition of g'

$$g' = \frac{(B_0 W)^{2/3}}{z} \quad (17)$$

to get equation (9) for r_e . Here we take a similar approach but argue that g' should take a different form. If we assume

that the descending curtain of dense fluid has width W and height H during a descent time $t < 1/f$, then conservation of buoyancy implies that

$$\frac{\partial}{\partial t}[Wg'H] = B_0 W, \quad (18)$$

$$[Wg'H] = B_0 W t. \quad (19)$$

These apply for $t < t_s$ only, which in our case is also $t < 1/f$. These lead to a new equivalence for g'

$$g' \sim \frac{B_0 W t}{WH} \sim \frac{B_0 t}{H}, \quad (20)$$

where g' is an areal average buoyancy anomaly of the salt plume. Using this definition of g' in R_d (equation (8)) leads to

$$R_d = \left(\frac{B_0}{f^3}\right)^{1/2} (f t_s)^{1/2}, \quad (21)$$

which for $t_s = 1/f$ becomes

$$R_d = \left(\frac{B_0}{f^3}\right)^{1/2}, \quad (22)$$

a quantity previous called l_{rot} and z_c [*Whitehead et al.*, 1996; *Jones and Marshall*, 1992]. Here, however, R_d represents a horizontal eddy length scale, in contrast to its previous interpretation of a vertical length scale for rotational arrest of descending plumes. On the basis of an examination of our numerical results it appears that the eddies grow to this length scale at $\sim t = t_s$ and subsequently retain this scale. It is important to realize that this definition of R_d assumes that W and H are constant in the convecting fluid, which may not be true after the fluid has begun to spread along the bottom. Thus, for shallow fluids in which the convecting fluid hits the bottom well before the first inertial period, this may not hold. This assumption also may not be true for times $t \gg \frac{1}{f}$, where the shape of the spreading fluid may need to be taken into account. Lead convection represents a special case where the duration of the buoyancy forcing is often close to the inertial period, and in that sense, R_d being l_{rot} may not be a general result. This result is in qualitative agreement with our numerical results that suggest eddy scale is most sensitive to B_0 . As section 4.8 shows, however, eddy size in our numerical experiments has a secondary dependence on lead width W that this scaling neglects.

[45] We can now compare the eddy radius obtained in these numerical experiments (Table 1, column 9) with those predicted by the scaling arguments (Table 1, column 8) proposed by *Bush and Woods* [1999]. In general, eddy radii found here are qualitatively similar to those suggested by equation (9) for comparable values of B_0 , width W , and duration of buoyancy forcing t_s .

[46] Despite this approximate agreement between laboratory and numerical results, the numerical eddy scales appear to have different parametric sensitivities than do the laboratory eddy scales. The numerical results indicate

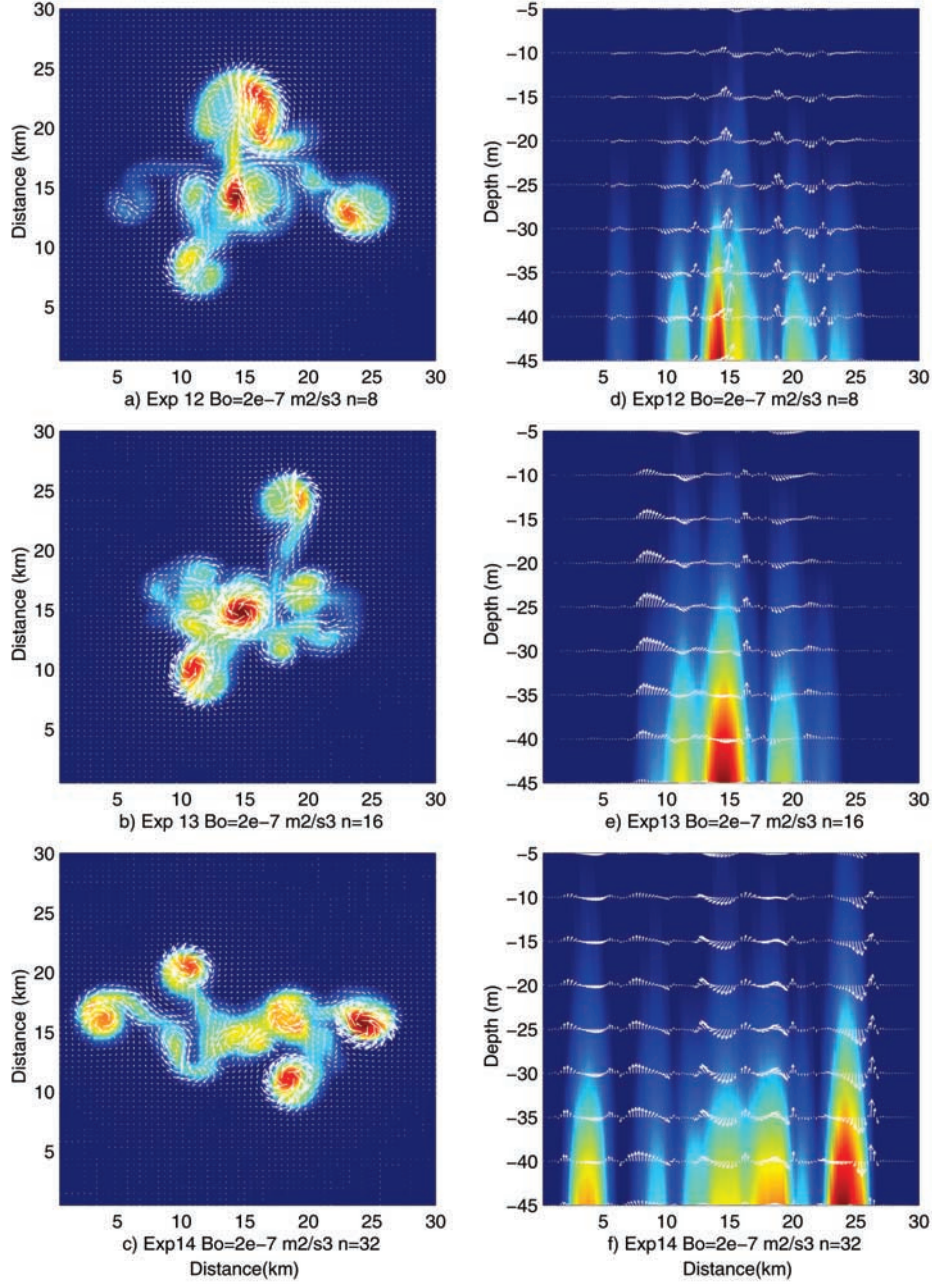


Figure 7. Sensitivity to along-lead variations in lead width (equation (16), experiments 12–14). In the left column, salinity anomaly at $z = -37.5$ m and at $t = 8$ days; in the right column, salinity anomaly at $y = 15$ km (source centerline) at $t = 8$ days. (a and d) $m = 8$; (b and e) $m = 16$; (c and f) $m = 32$ in equation (16). ΔS ranges from 0.001 (blue) to 0.05 (Figure 7a and 7d), 0.05 (Figure 7b and 7e), 0.04 (Figure 7c and 7f).

that eddy radius is most sensitive to the magnitude of the buoyancy forcing (experiments 1–3) than to other varied parameters. There is a slight dependence of eddy size on source width W (compare experiments 4–6), and the eddy radius is least sensitive to layer thickness H (experiments 10 and 11) and the duration timescale, t_s (experiments 7–9). This latter result in particular appears at odds with the prediction of equation (9), which indicates that eddy size should scale with this timescale.

[47] In Figure 8, we have plotted the experimental eddy scale seen in these numerical results (Table 1) versus those predicted by equation (9) [Bush and Woods, 1999]. It is inappropriate to expect equation (9) to predict the eddy scale for finite width leads (experiments 4–6), as it was developed for the line source case. Equation (9) does suggest, however, that eddy size is sensitive to buoyancy flux (B_0 , experiments 1–3), width (W , experiments 4–6), and duration of forcing (t_s , experiments 7–9). In general,

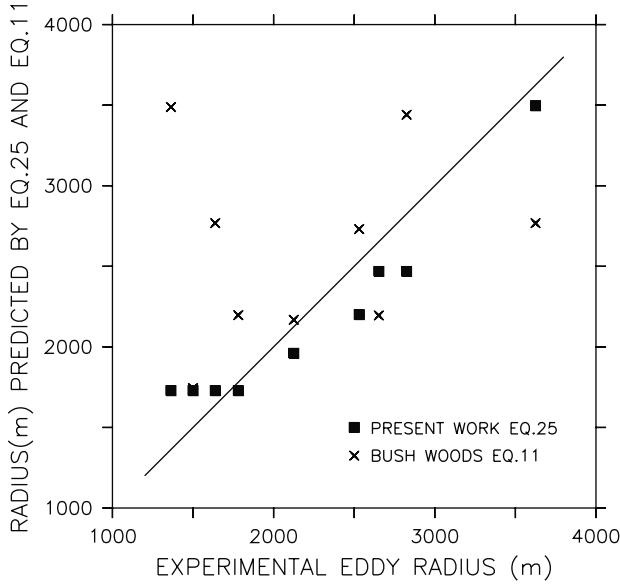


Figure 8. Eddy radius r_e from numerical experiments 1–9 (Table 1) versus the *Bush and Woods* [1999] equation (9). The solid line represents a perfect correlation.

equation (9) slightly overpredicts the eddy size seen in numerical experiments here but slightly underpredicts the eddy size for increased values of B_0 . Our eddy sizes do not increase with duration t_s of the forcing as equation (9) suggests. The line shown on Figure 8 is a fit to the numerical data, which indicates that eddy size is approximated by

$$L_e = 4.0 \left(\frac{B_0}{f^3} \right)^{1/2} \left(\frac{W}{H} \right)^{1/6}, \quad (23)$$

indicating the primary dependence of eddy size on the Rossby radius of deformation ($= l_{rot}$) and the secondary dependence on the width W of the buoyancy source. In summary, the numerical experiments here suggest a greater dependence of eddy size on magnitude of the buoyancy flux, a weak dependence on source width, and no dependence on duration of the forcing. In general, however, the fact that the laboratory and numerical results are within a factor of 2 of each other indicates an encouraging qualitative agreement.

4.8. Smagorinsky Mixing

[48] We have also implemented Smagorinsky mixing [Smagorinsky, 1963] in the present model and briefly consider the impact of using that mixing scheme on the results presented in the previous sections. In the biharmonic dissipation and diffusion cases (experiments 1–13) we have used different values of B_h and B_s in the horizontal and vertical terms. For the physical scales of interest the required grid cells are much larger in the horizontal than in the vertical, and hence vertical values of B_h are reduced by the factor of $(\Delta z/\Delta x)^4$. This difference in horizontal and vertical mixing coefficients also reflects the different horizontal and vertical eddy length scales in rotationally dominated turbulence. Experiments in which the vertical term is not reduced in this manner are overly viscous, causing

vertical uniform salt concentrations, reduced entrainment near the surface, less lateral shear instability, and hence fewer, if any, vortices. Because that result disagrees with the laboratory experiments, the choice of vertical B_h less than horizontal B_h seems reasonable.

[49] In contrast to biharmonic mixing, Smagorinsky mixing assumes isotropic mixing and generates a more physically based mixing coefficient depending on local fluid shears. For the same reasons expressed for biharmonic cases, however, the Smagorinsky mixing coefficients in the vertical were reduced by a factor of $(\Delta z/\Delta x)^4$ from isotropic values. This makes magnitudes of vertical mixing in the biharmonic and Smagorinsky mixing cases comparable.

[50] Figure 9 (experiment 15) shows salinity and vorticity distributions for the base case experiment (experiment 1, Figures 1 and 2) with the inclusion of Smagorinsky mixing. A comparison of these results with those shown in Figure 1 indicates that the instability mechanism is still present and that dipole features are shed from each end of the buoyancy source with approximately the same timing. A single high-salinity anticyclone remains in the center of the domain in this experiment in contrast to additional dipole formation in experiment 1.

[51] An examination of the magnitude of Smagorinsky mixing coefficients was conducted to determine their magnitude relative to the mixing associated with biharmonic dissipation in the previous experiments. A contour plot of these values indicates that the Smagorinsky scheme generates large local values of mixing where local maxima in the shear field occur. This results in a very patchy field of mixing coefficients with maximum values of $1.2 \text{ m}^2 \text{ s}^{-1}$. An average value of $0.2 \text{ m}^2 \text{ s}^{-1}$ occurs elsewhere in fluid where eddies occur. For comparison, the biharmonic coefficient of $B_h = 0.2 \times 10^5 \text{ m}^4 \text{ s}^{-1}$, when scaled by the grid cell size, leads to a Laplacian mixing coefficient of $A_h = 2 \text{ m}^2 \text{ s}^{-1}$,

$$A_h = 0.25 \frac{B_h}{(\Delta x)^2}. \quad (24)$$

[52] This formula for translation between Laplacian and biharmonic mixing values was found to give comparable results in numerical experiments given by *Smith and Morrison* [1993]. The Smagorinsky scheme thus generates mixing values that are roughly in agreement with those generated by biharmonic mixing but applies locally enhanced mixing in high-shear regions of the fluid, leading to the smearing of vortex edges seen in Figure 9.

[53] Smagorinsky mixing thus produces differences in the details of the mixing when compared with the previous cases with biharmonic mixing, but the basic instability and formation of eddies along the lead is unaltered by the inclusion of this mixing formulation. This suggests that the dynamics of eddy formation in leads is illustrated in previous laboratory experiments and is captured in numerical experiments here and the instability and eddy generation process dominates the flow field signature over the details of the mixing scheme (at least for the timescales of interest here). This implies that the eddies seen in the present experiments might be seen in the geophysical problem of convectively driven flows under leads in sea ice. The inclusion of Smagorinsky mixing may produce different eddy spin-down times for the eddies and thus may

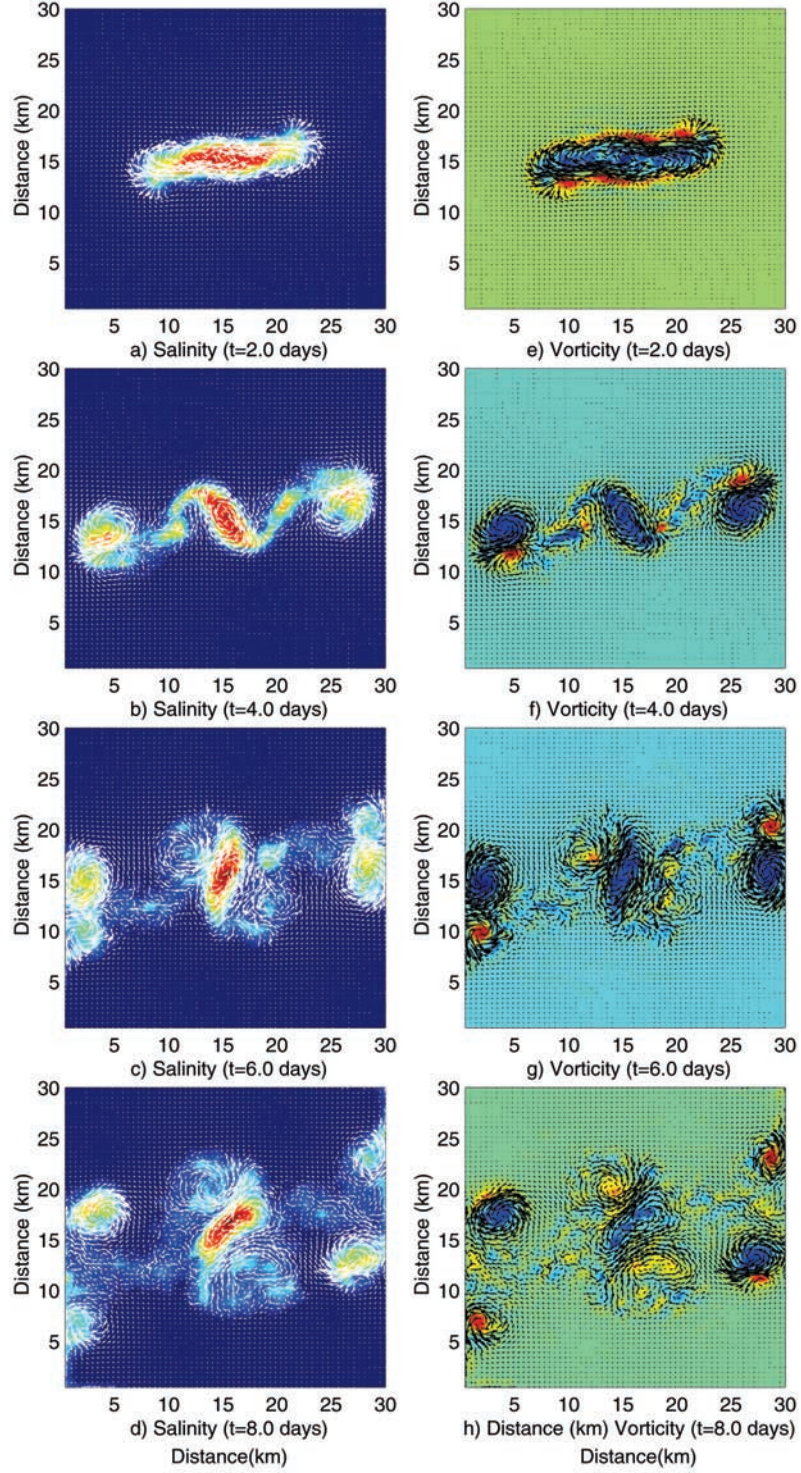


Figure 9. Experiment 15 (experiment 1 but with Smagorinsky rather than biharmonic mixing). In the left column, salinity anomaly at $z = -37.5$ m and at $t = 2, 4, 6,$ and 8 days; In the right column, relative vorticity ζ (s^{-1}) in the z -direction at $y = 15$ km (source centerline) at $t = 2, 4, 6,$ and 8 days. ΔS ranges from 0.001 (blue) to 0.15 (red), and ζ ranges from $-6.0 \times 10^{-4} \text{ s}^{-1}$ (blue) to $6.0 \times 10^{-4} \text{ s}^{-1}$ (red).

have implications for the lifetimes of Arctic eddies, but we have not investigated this.

5. Summary and Conclusions

[54] We have numerically explored the generation of eddies by convective instability in leads in sea ice associated with brine rejection in winter. The sensitivity of the eddy generation process to a range of lead parameters, including lead width, duration of lead opening, buoyancy flux, and mixed-layer depth were considered. A generally robust eddy length scale (radius) of $O(1.5\text{--}3.5\text{ km})$ is seen in most experiments. We have compared our results with those obtained for line segment sources in laboratory experiments [Bush and Woods, 1999], despite the fact that the source width to fluid depth ratio (W/H) places their experiments in rather different regimes. The resulting eddy radius here is somewhat smaller than predicted by the scaling (equation (9)) presented by Bush and Woods [1999].

[55] Despite the general agreement with this scale for typical lead generation periods $t_s \sim 24$ hours, we find that longer forcing periods t_s do not lead to larger eddy sizes, as Bush and Woods [1999] predict. This formula also suggests that eddy size should increase as lead width increases. Our numerical experiments with increased W do lead to the generation of slightly larger eddies. The number of eddies, however, goes up with lead width also. Bush and Woods [1999] determine the number of eddies produced in a given case by $n \sim Lr_e^{-1}$. Results here suggest that the number of eddies produced is more likely to be proportional to AL_e^{-1} , where A is the lead surface area and L_e is the eddy length scale. In summary, the eddy radius in these experiments is most sensitive to the magnitude of the buoyancy forcing B_0 , with a secondary dependence on lead width W and little or no dependence on duration of forcing t_s .

[56] We have thus extended the results of Bush and Woods [1999] to include the effects of finite source width, not explicitly treated in their study. By varying B_0 and W independently in the experiments, we have shown that the resulting eddy scale depends not simply on their product, as equation (9) suggests, but that there is a separate width dependence which should be incorporated in future scalings. Our results also suggest that the duration of the buoyancy source does not control eddy size. Despite these differences, our numerical results for eddy size are generally within a factor of 2 predicted by their laboratory experiments. This is a rather encouraging agreement, given the different nature of the laboratory and numerical methods used.

[57] It is also incorrect to conclude that all eddies generated in leads should be anticyclonic. Some of the salt-containing eddies seen in these experiments are, for example, cyclonic and are spun up as secondary circulation cells after descending plumes drive upward return flows. Anticyclones do, however, contain the majority of the salt and appear to persist longer than the secondary cyclones. It seems unlikely that the anticyclones generated in these lead simulations are related to the ones that have been observed by Manley and Hunkins [1985]. The anticyclones discussed by Manley and Hunkins [1985] are deeper in the Arctic halocline and have larger dimensions ($O(10\text{ s km})$) than predicted here.

[58] Because the nonhydrostatic ocean model is not coupled to an ice model, this prescribed forcing does not

allow feedback between the ocean and an evolving ice cover. It is possible, for example, that time variability in the location of the buoyancy flux as the ice moves could locally enhance eddy development in a way not seen in the present simulations. Further simulations should allow for this feedback between evolving ocean circulation field and ice edge variations.

[59] In general, lead convection is also driven by a moving source of buoyancy. Near-surface, ice-water momentum flux provided by the moving ice produces a shear zone at the ice-water interface that also modifies the diffusive growth of the unstable buoyancy layer. Morison *et al.* [1992] have proposed that this effect can be quantified in terms of lead width, ice-water speed, and buoyancy flux anticipated in a nondimensional quantity known as the lead number. Although we have not considered moving buoyancy sources here, this problem was considered numerically in two dimensions by Smith and Morison [1998], where support for this nondimensional scaling was found. For typically observed values of buoyancy flux, lead width, and ice-water speed, mixing by convective overturning and boundary layer mixing by ice-water momentum flux are equally important in mixing salt into the Arctic mixed layer.

Notation

α	salinity expansion coefficient psu^{-1} .
A_I	Smagorinsky momentum diffusion coefficient.
$B_0 W$	buoyancy flux per unit length $\text{m}^3 \text{s}^{-3}$.
B_0	buoyancy flux per unit area $\text{m}^2 \text{s}^{-3}$.
B_h	biharmonic momentum dissipation coefficient $\text{m}^4 \text{s}^{-1}$.
B_S	biharmonic salinity diffusion coefficient = B_h .
Δx	model horizontal resolution.
Δz	model vertical resolution.
Δt	model time step.
f	Coriolis parameter = 2Ω .
F_0	total buoyancy flux $\text{m}^4 \text{s}^{-3}$.
F_S	brine rejection rate $\text{kg m}^{-2} \text{s}^{-1}$.
\mathbf{F}_{DISS}	momentum dissipation.
\mathbf{F}_{DIFF}	salinity diffusion.
g	gravitational acceleration.
g'	reduced gravity based on buoyancy anomaly.
H	Arctic mixed layer depth.
\mathbf{k}	unit vector in the vertical direction.
K_I	Smagorinsky salinity diffusion coefficient.
λ_L	along-lead perturbation wavelength.
λ_s	e-folding scale for salt source term.
L	lead length.
L_e	eddy length scale (radius) in experiments 1–15.
n	number of eddies.
Ω	planetary rotation rate.
Q	volume flux of fluid into the domain $\text{m}^3 \text{s}^{-1}$.
Q_s	source term for salt.
r_e	eddy radius predicted by Bush and Woods [1999].
R_d	Rossby radius of deformation.
t_{Eady}	Eady instability timescale.
t_s	duration of buoyancy forcing.
W	lead width.
ζ	relative vorticity = $\frac{\partial v}{\partial x} - \frac{\partial u}{\partial y}$.
z_c	plume rotational length scale = $\left(\frac{B_0}{f^3}\right)^{1/2} (= \ell_{\text{rot}})$.

[60] **Acknowledgments.** DCSIV was supported by the Office of Naval Research, High Latitude Processes, NSF grant 0084310 and by NASA contract NAGW 4213. Support for convection work for JW. comes from the NOAA VENTS program. NOAA/Pacific Marine Environmental Laboratory Contribution 2288.

References

- Akitomo, K., N. Imasato, S. Yamashita, T. Awaji, and G. Yu, A numerical study on scale selection of convection in a shallow sea, *Cont. Shelf. Res.*, **12**, 451–469, 1992.
- Bush, J. W., and A. W. Woods, Vortex generation by line plumes in a rotating stratified fluid, *J. Fluid Mech.*, **388**, 289–313, 1999.
- Chapman, D. C., and G. Gawarkiewicz, Shallow convection and buoyancy equilibration in an idealized coastal polynya, *J. Phys. Oceanogr.*, **27**, 555–566, 1996.
- Ching, C. Y., H. J. S. Fernando, and Y. Noh, Interaction of a negatively buoyant line plume with a density interface, *Dyn. Atmos. Oceans*, **19**, 367–388, 1993.
- Colomer, J., B. Boubnov, and H. J. S. Fernando, Turbulent convection from isolated sources, *Dyn. Atmos. Oceans*, **30**, 125–148, 1999.
- Eady, E. T., Long waves and cyclone waves, *Tellus*, **1**, 33–52, 1949.
- Fernando, H. J. S., and C. Y. Ching, Effects of background rotation on turbulent line plumes, *J. Phys. Oceanogr.*, **23**, 2125–2129, 1993.
- Fernando, H. J. S., and D. C. Smith, IV, Vortex structures in geophysical convection, *Eur. J. Mech.*, **20**, 437–470, 2001.
- Griffiths, R. W., P. D. Killworth, and M. E. Stern, Ageostrophic instability of ocean currents, *J. Fluid Mech.*, **117**, 343–377, 1982.
- Harlow, F. H., and J. E. Welch, Numerical calculation of time-dependent viscous incompressible flow of fluid with a free surface, *Phys. Fluids*, **8**, 2182–2189, 1965.
- Helfrich, K. R., and T. M. Battisti, Experiments on baroclinic vortex shedding from hydrothermal plumes, *J. Geophys. Res.*, **96**, 12,511–12,538, 1991.
- Jones, H., and J. Marshall, Convection with rotation in a neutral ocean: A study of open ocean deep convection, *J. Phys. Oceanogr.*, **23**, 1009–1039, 1992.
- Kozo, T. L., Initial model results for Arctic mixed layer circulation beneath a refreezing lead, *J. Geophys. Res.*, **88**, 2926–2934, 1983.
- Lavelle, J. W., and D. C. Smith IV, Effects of rotation on convective plumes from line segment sources, *J. Phys. Oceanogr.*, **26**, 863–872, 1996.
- Manley, T. O., and K. Hunkins, Mesoscale eddies of the Arctic Ocean, *J. Geophys. Res.*, **90**, 4911–4930, 1985.
- Maxworthy, T., and S. Narimousa, Unsteady, turbulent convection into a homogeneous, rotating fluid with oceanographic applications, *J. Phys. Oceanogr.*, **24**, 865–887, 1994.
- Maxworthy, T., Convection into domains with open boundaries, *Annu. Rev. Fluid Mech.*, **29**, 327–371, 1997.
- Morison, J. H., Forced internal waves in the Arctic, Ph.D. thesis, University of Washington, Seattle, 1980.
- Morison, J. H., M. G. McPhee, T. B. Curtin, and C. A. Paulson, The oceanography of winter leads, *J. Geophys. Res.*, **97**, 11,199–11,218, 1992.
- Morison, J. H., and M. G. McPhee, Lead convection measured with an autonomous underwater vehicle, *J. Geophys. Res.*, **103**, 3257–3281, 1998.
- Morton, B. R., G. I. Taylor, and J. S. Turner, Turbulent gravitational convection from maintained and instantaneous sources, *Proc. R. Soc. London, Ser. A*, **234**, 1–23, 1956.
- Noh, Y., H. J. S. Fernando, and Y. Ching, Flow induced by the impingement of a thermal on a density interface, *J. Phys. Oceanogr.*, **22**, 1207–1220, 1992.
- Ou, H. W., Time-dependent model of a coastal polynya, *J. Phys. Oceanogr.*, **18**, 584–590, 1988.
- Send, U., and J. Marshall, Integral effects of deep convection, *J. Phys. Oceanogr.*, **25**, 855–872, 1995.
- Smagorinsky, J., General circulation experiments with primitive equations, I, The basic experiment, *Mon. Weather Rev.*, **91**, 99–164, 1963.
- Smith, D. C., IV, and J. H. Morison, A numerical study of haline convection beneath leads in sea ice, *J. Geophys. Res.*, **98**, 10,069–10,087, 1993.
- Smith, D. C., IV, and J. H. Morison, Nonhydrostatic haline convection beneath leads in sea ice, *J. Geophys. Res.*, **103**, 3233–3247, 1998.
- Turner, J. S., *Buoyancy Effects in Fluids*, 367 pp., Cambridge Univ. Press, New York, 1973.
- Visbeck, M., J. Marshall, and H. Jones, Dynamics of isolated convective regions in the ocean, *J. Phys. Oceanogr.*, **101**, 1723–1734, 1996.
- Whitehead, J. A., J. Marshall, and G. E. Hufford, Localized convection in rotating stratified fluid, *J. Geophys. Res.*, **101**, 25,705–25,721, 1996.

D. C. Smith IV, Department of Mechanical and Aerospace Engineering, Arizona State University, Tempe, AZ 85287, USA. (dcsiv@asu.edu)

J. W. Lavelle, Pacific Marine Environmental Laboratory, NOAA, 7600 Sand Point Way NE, Seattle, WA 98115, USA. (lavelle@pmel.noaa.gov)

H. J. S. Fernando, Department of Mechanical and Aerospace Engineering, Arizona State University, Tempe, AZ 85287, USA. (j.fernando@asu.edu)